Intensity interferometry of P Cygni in the Hα emission line: towards distance calibration of LBV supergiant stars

J. -P. Rivet, A. Siciak, E. S. G. de Almeida, F. Vakili, A. Domiciano de Souza, M. Fouché, O. Lai, D. Vernet, R. Kaiser, W. Guerin

Monthly Notices
of the
ROYAL ASTRONOMICAL SOCIETY

MNRAS **494,** 218–227 (2020)
Advance Access publication 2020 February 27

doi:10.1093/mnras/staa588

Intensity interferometry of P Cygni in the H α emission line: towards distance calibration of LBV supergiant stars

J.-P. Rivet,[1]★ A. Siciak,[2] E. S. G. de Almeida,[1] F. Vakili,[1,3] A. Domiciano de Souza,[1] M. Fouché,[2] O. Lai ,[1] D. Vernet,[4] R. Kaiser[2] and W. Guerin [2]★

[1]*Laboratoire Lagrange, Observatoire de la Côte d'Azur, CNRS, Université Côte d'Azur, F-06304 Nice, France*
[2]*Institut de Physique de Nice, CNRS, Université Côte d'Azur, F-06560 Valbonne, France*
[3]*Department of Physics, Shahid Beheshti University, Shahid Shahriari Square, Tehran 19839 69411, Iran*
[4]*UMS Galilée, Observatoire de la Côte d'Azur, CNRS, Université Côte d'Azur, F- 06304 Nice, France*

Accepted 2020 February 25. Received 2020 February 20; in original form 2019 December 10

ABSTRACT

We present intensity interferometry of the luminous blue variable P Cyg in the light of its H α emission performed with 1 m-class telescopes. We compare the measured visibility points to synthesized interferometric data based on the CMFGEN physical modelling of a high-resolution spectrum of P Cyg recorded almost simultaneously with our interferometry data. Tuning the stellar parameters of P Cyg and its H α linear diameter, we estimate the distance of P Cyg as 1.56 ± 0.25 kpc, which is compatible within 1σ with 1.36 ± 0.24 kpc reported by the *Gaia* DR2 catalogue of parallaxes recently published. Both the values are significantly smaller than the canonic value of 1.80 ± 0.10 kpc usually adopted in literature. Our method used to calibrate the distance of P Cyg can apply to very massive and luminous stars both in our Galaxy and neighbouring galaxies, and can improve the so-called wind momentum–luminosity relation that potentially applies to calibrate cosmological candles in the local Universe.

Key words: techniques: interferometric – stars: distances – stars: massive – stars: winds, outflows.

1 INTRODUCTION

The purpose of this paper is to show that, even with its present limitations, intensity interferometry can provide new and useful information on the fundamental stellar parameters and the mechanisms that govern the physics of massive stars and their mass-loss : more precisely on the luminous blue variable (LBV) archetype star P Cyg (HD193237) (Najarro 2001).

Intensity interferometry (hereafter II), as imagined by Hanbury Brown and Twiss in the 1950s (Hanbury Brown & Twiss 1956), culminated in the early 1970s by providing the first systematic catalogue of the angular diameter (in the visible) of 32 stars observed with the Narrabri 200 m-baseline interferometer (Hanbury Brown, Davis & Allen 1974). In addition to this, Hanbury Brown and his team explored different phenomenological effects, such as flattening of rapidly rotating stars, close binary stars and their parameters (Herbison-Evans et al. 1971), scattering effects occurring in the massive wind of blue supergiants and emission carbon line extent of a Wolf–Rayet star (Hanbury Brown et al. 1970). An extensive review of these experiments is described by Hanbury Brown in his book on the Narrabri interferometer (Hanbury Brown 1974), which stopped operating in the early seventies. More contemporary, Cherenkov arrays of telescopes have been considered to revive II with much larger collectors in size and much longer baselines, aiming at stellar surface imaging by aperture synthesis interferometry on a much broader class of targets (Dravins 2016; Kieda et al. 2019a, b). Successful demonstrations of II with Cherenkov telescopes have been reported very recently (Matthews & LeBohec 2019; Acciari et al. 2020). In this context, our group started a number of pilot experiments in 2016 using two modest 1 m size optical telescopes. After the successful observations of temporal and spatial bunching on a few bright stars at 780 nm (Guerin et al. 2017, 2018; Lai et al. 2018; Rivet et al. 2018), we decided to observe emission-line stars. The LBV star P Cyg is a very good candidate due to its strong H and He emission lines.

In the following, we shortly discuss the photometric and spectral variability of P Cyg, especially for its H α line that is relevant to our II observations. We then summarize the three long-baseline interferometric studies available in the literature that shed light on the present results.

Along with η Car, P Cyg is the brightest LBV star in the sky, having undergone a giant eruption in the 17th century and for which evolutionary change has been recorded from its apparent magnitude by Lamers & de Groot (1992) over three centuries. More recently, P Cyg was studied by Markova et al. (2001) using *U*, *B*,

★ E-mail: rivet@oca.eu (J-PR); william.guerin@inphyni.cnrs.fr (WG)

V photometry and H α emission, including equivalent width (EW) monitoring over 13.8 yr from 1985 to 1999. These authors find that P Cyg undergoes a slow 7.4 yr variation in its V magnitude, where the star becomes redder when it brightens, and vice versa. They also show that the H α EW changes in correlation with the photometric trend and conclude that the variable wind increases the photospheric radius while the effective temperature is decreasing. Markova et al. (2001) concluded that the wind mass-loss rate of P Cyg increased of ∼19 per cent over a period of about 7 yr. This increase in mass-loss rate implies an apparent stellar radius (pseudo-photosphere) larger by ∼7 per cent. Thus, angular diameter observations of this star also need to be monitored by spectrometry of the H α line and simultaneous photometry (Pollmann & Vollmann 2013) in order to correctly analyse and interpret the interferometric data. This work meets the H α spectroscopy criterion.

Milliarcsec (mas) resolution observations of P Cyg trace back to GI2T spectrally resolved interferometry based on visibility and differential phase of the H α emission line (Vakili et al. 1997). These quantities were determined as a function of the Doppler-shift across the H α line profile and gave the first angular diameter of P Cyg's envelope as well as a limit to its extent in He I line. In addition, the signature of an asymmetry in the wind of P Cyg was concluded from a differential phase occurring at the blue absorption component of the H α line. It is worth noting that Vakili et al. (1997) estimated the diameter of P Cyg in H α as 5.52 ± 0.47 mas assuming a simple equivalent uniform disc, without separating the star photosphere and its envelope emission. This single shot observation and study of P Cyg was followed in 1997 by adaptive optics imaging in the H α line through a 1 nm filter and in its continuum vicinity with a 1.5 m telescope, corresponding to 0.1 arcsec diffraction limit resolution (Chesneau et al. 2000). This adaptive optics imaging aimed at first to determine the large-scale extent of P Cyg's envelope as it had been previously witnessed by *Hubble Space Telescope* observations (Nota et al. 1995), and secondly, to detect, if possible, the propagation after 4 yr of the heterogeneities of P Cyg's wind detected by the GI2T. The latter expectation was roughly confirmed whilst it was also clearly confirmed that any high angular resolution observation of P Cyg should consider the central LBV engine, its mass-loss envelope out to thousands of stellar radii, even though dilution factor would make this a high-contrast imaging challenge.

P Cyg was then observed between 2005 and 2008 with the Navy Precision Optical Interferometer (NPOI) interferometer (Balan et al. 2010) with simultaneous spectroscopy to relate any angular diameter variation with the H α line profile and/or emission strength. These observations used a much broader filter than the above-mentioned studies and modelling of the envelope was conducted for the equivalent H α width emission using different circular shapes. Finally, the authors concluded that the data are best fitted with a double Gaussian structure of 5.64 ± 0.21 and 1.80 ± 0.13 mas for P Cyg's envelope. In addition, they found no asymmetry of the envelope and less than 10 per cent variation in size between 2005 and 2008. To make NPOI results comparable to previous GI2T measures, Balan et al. (2010) also considered the simple model of a uniform disc for P Cyg's emission envelope including indifferently the photosphere as well as its envelope. They found uniform disc angular diameters ranging from 8.4 to 10.2 mas on the seasonal observations between 2005 and 2008, a result that significantly differs from those by the GI2T single baseline data. Balan et al. finally concluded that this discrepancy might result from photospheric flux variability and opacity changes through the multiple wind layers of P Cyg.

More recent long baseline interferometry of P Cyg, covering the period of 2006–2010, has been reported by Richardson et al. (2013) using the CHARA interferometer at Mount Wilson. These observations were accompanied by simultaneous infrared (IR) photometry and spectroscopy to monitor any change in the angular size of P Cyg related to the activity at the base of the wind and its impact on eventual fine structures within the mass-loss. These observations differ from previous studies since they have been performed in the IR at 1.6 μm (*H* band), but can still compare to GI2T and NPOI observations. A first important issue of CHARA-MIRC conclusions consists of setting an angular diameter of 0.96 ± 0.02 mas for the wind component of P Cyg at its photospheric base with about 45 per cent of the *H*-band flux. This angular diameter is significantly larger than the 0.41 mas (Najarro, Hillier & Stahl 1997) that was adopted for P Cyg photospheric diameter used by the GI2T paper for instance (Vakili et al. 1997). Additionally, multiple baseline performed with CHARA-MIRC at two epochs in 2010 August and 2011 September were used by Richardson et al. (2013) to reconstruct an image of P Cyg from the Earth rotation synthesis data. Furthermore, these authors used the non-LTE radiative transfer code CMFGEN (spherically symmetric wind) to compare the observed visibility curve of P Cyg to the predicted one. Whilst no significant departure was found from circular symmetry, Richardson et al. concluded that P Cyg is best explained by a two-component model consisting of a uniform disc photosphere unresolved by CHARA at its 0.56 mas resolution in the *H* band and a 0.96 ± 0.02 mas Gaussian halo emitted from the inner regions of the stellar wind of P Cyg. The difference between this result and the 5.5 mas size found by Vakili et al. (1997) can be explained by a larger wind-emitting volume because of its higher optical depth in H α diameter. Besides these interferometric studies, such a spherically symmetric wind around P Cyg is also supported by H α spectroscopy (Richardson et al. 2011).

Due to their limited spatial frequency content, interferometric observations require a model for their interpretation and as shown by the review of these high-resolution results, models that introduce the least amount of a priori information (e.g. uniform disc or Gaussian profile) are usually chosen, yielding limited information, such as the apparent diameter. For our II campaign reported herein, we chose an alternative approach, using the best physical parameters of P Cyg from the CMFGEN code (Hillier & Miller 1998) that reproduce high-resolution spectrometry of the star obtained quasi-simultaneously to our II campaign, to compute the intensity distribution (and its associated visibility) of P Cyg in the emission line, which can be directly compared to our measured visibilities. This additional information constrains the physical size of P Cyg and allows us to estimate the only remaining free parameter, which is its distance. We believe that the association of physical modelling of stellar parameters of LBVs from spectroscopy with interferometric observations has the potential to be a powerful method to refine the first few rungs of the cosmological distance ladder.

The paper is organized as follows. In the next section, we describe our experimental setup and the observing conditions. In Section 3, we show the results of our single-telescope observations, which can be used to calibrate the visibility at zero baseline. This also corresponds to measuring the *temporal* intensity correlation, related to the width of the spectral line. Then, in Section 4, we present the *spatial* intensity correlation measurements performed with two telescopes separated by 15 m. We observe a reduction of the contrast of the correlation, demonstrating a partial resolution of the emitting envelope. Finally, in Section 5, we present our CMFGEN best model to compare the expected and the measured visibilities using the star

distance as the only free parameter. We then conclude and draw some perspectives.

2 EXPERIMENTAL SETUP

2.1 Principle

Stellar intensity interferometry is based on the measurement of the temporal and spatial correlations between the fluctuations of light collected by two telescopes distant by r. The quantity of interest is the intensity correlation function given by

$$g^{(2)}(r,\tau) = \frac{\langle I(t,0)I(t+\tau,r)\rangle}{\langle I(t,0)\rangle\,\langle I(t,r)\rangle}, \quad (1)$$

where the brackets denote the average over time t. For a classical (non-quantum) source of light, correlations are maximum at zero delay ($\tau = 0$) and zero separation ($r = 0$). For a 'chaotic' (incoherent) source, Gaussian statistics on the field fluctuations leads to $g^{(2)}(0, 0) = 2$. On the contrary, at large separation r and delay τ, the fluctuations become uncorrelated and the $g^{(2)}(\tau, r)$ tends to 1. The decrease from 2 to 1 of the $g^{(2)}$ function with the time delay τ is related to the temporal coherence time τ_c, which is inversely proportional to the spectrum width. The decrease of the $g^{(2)}$ function with the separation r is related to the spatial coherence of the source, i.e. the usual 'visibility' $V(r)$ measured in direct (amplitude) stellar interferometry (Labeyrie, Lipson & Nisenson 2006).

We can therefore use the following equation, valid for chaotic light (Loudon 1973),

$$g^{(2)}(r,\tau) = 1 + |V(r)|^2 |g^{(1)}(\tau)|^2, \quad (2)$$

where $g^{(1)}(\tau)$ is the first-order (field–field) temporal correlation function, related to the optical spectrum $S(\omega)$ by a Fourier transform (Wiener–Khinchin theorem),

$$S(\omega) \propto \mathfrak{F}[g^{(1)}(\tau)]. \quad (3)$$

Similarly, the visibility is related to the brightness distribution of the source by a Fourier transform, like in direct interferometry. Note that we suppose here that the detected light is polarized, otherwise it amounts at reducing the visibility by a factor 2.

In practice, the coherence time τ_c, which gives the width of the $g^{(2)}(\tau)$ function, is often too short to be resolved by the electronic detection chain, whose finite timing resolution τ_{el} introduces an uncertainty on the arrival time of each photon. In that case, the measured 'bunching peak' $g^{(2)}(\tau)$ has a width given by $\tau_{el} \gg \tau_c$, and a height, which we call the contrast $C = g^{(2)}(0, 0) - 1$, reduced from $C = 1$ to $C \sim \tau_c/\tau_{el} \ll 1$. This contrast has to be calibrated as it corresponds to the maximum (zero-baseline) squared visibility.

2.2 Instrumental setup

Our experimental setup has been described in detail in previous publications (Guerin et al. 2017, 2018). In short, it consists first in a coupling assembly (CA) set at the focus of the telescope, which allows injecting light into a multimode fiber (MMF) of diameter 100 µm. Then, we use single-photon avalanche photodiodes (SPADs) to detect light in the photon-counting regime and digital electronics in order to compute the $g^{(2)}$ function. The SPADs have a timing jitter of $\simeq$450 ps each, which gives a temporal resolution $\tau_{el} \simeq \sqrt{2} \times 450 \simeq 640$ ps for the correlation function.

Compared to our previous experiments (Guerin et al. 2017, 2018), we have modified the CA in order to collimate the optical beam before its transmission through the filter, in order to have a more precise control on the filter width and central wavelength. This is indeed more critical when one wants to select a specific spectral line. The new CA is described in Fig. 1. As previously, there is first a dichroic mirror that reflects part of the light to a guiding camera. The transmitted light is then collimated by a diverging lens (focal length $f = -50$ mm). The collimated beam goes through a filter of width $\Delta\lambda = 1$ nm (FWHM), centred at $\lambda = 656.3$ nm (Hα line), with a peak transmission of 95 per cent, and then to a polarizer, before being focused by a converging lens ($f = 20$ mm) on the fiber tip.

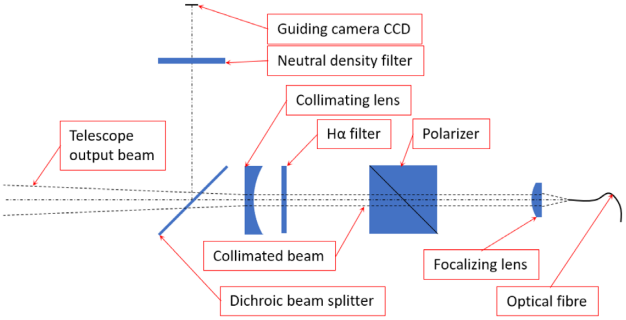

Figure 1. Scheme of the coupling assembly set at the telescope focus in order to perform spectral and polarization filtering, and injection into an MMF, which transports the light to the detection chain. The Hα 1 nm filter operates in nominal conditions, i.e. on a collimated beam.

The observations have been performed at the C2PU facility at the Plateau de Calern site of Observatoire de la Côte d'Azur (OCA). The two, quasi-identical, telescopes have a diameter of 1.04 m with an F/12.5 aperture in a Cassegrain configuration. With the CA, the total equivalent focal length is 5.2 m. The two CAs are identical and we have checked, using an artificial star in the lab, that they produce identical correlation functions.

2.3 Observation conditions

The observations of P Cyg were performed in 2018 August over eight nights. The main characteristics of the observing runs are summarized in Table 1.

The observing time was used in two configurations. In the first one, we used only one telescope (always the same), in order to measure the temporal intensity correlation function $g^{(2)}(\tau)$ at zero baseline, as in Guerin et al. (2017). In principle, the contrast of the correlation function allows calibrating the visibility measured with two telescopes, which is the second configuration we used, as in Guerin et al. (2018).

3 TEMPORAL INTENSITY CORRELATION

Performing intensity interferometry on an emission line puts an important constraint on the measurement procedure. Indeed, since the $g^{(2)}$ function depends on the spectrum, it is not possible to use a distant, unresolved star as calibrator for the visibility measurement, because this calibrator would have a different spectrum from the science target. For the same reason, it is not possible to calibrate the visibility with an artificial star in the laboratory, as in Guerin et al. (2018). As a consequence, there are two possibilities. The first is to measure the actual spectrum, use equations (2) and (3) and, knowing the temporal resolution of the detection chain, infer the expected bunching contrast for maximum visibility. The second is to perform a temporal intensity correlation measurement with

Table 1. Main circumstances for the observing runs performed on P Cyg over eight nights. 'Configuration' indicates the performed experiment, either $g^{(2)}(\tau)$ (single-telescope experiment) of $g^{(2)}(r)$ (two-telescope experiment). Begin and end dates are in UTC (*ISO* 8601 compact format). a is the airmass range. The seeing information is provided by the GDIMM instrument (Ziad et al. 2012; Aristidi et al. 2014) of the CATS station (Calern Atmospheric Turbulence Station) (Chabé et al. 2016). The numbers are given as median values over the whole nights.

Configuration	Begin	End	a	Seeing (arcsec)
$g^{(2)}(\tau)$	20180801*T*2102*Z*	20180802*T*0111*Z*	1.00–1.10	1.29
$g^{(2)}(\tau)$	20180802*T*2025*Z*	20180803*T*0154*Z*	1.00–1.18	0.66
$g^{(2)}(\tau)$	20180804*T*0040*Z*	20180804*T*0309*Z*	1.06–1.44	1.10
$g^{(2)}(\tau)$	20180806*T*1943*Z*	20180806*T*2205*Z*	1.02–1.22	0.56
$g^{(2)}(r)$	20180807*T*0054*Z*	20180807*T*0356*Z*	1.10–1.79	0.56
$g^{(2)}(r)$	20180807*T*2212*Z*	20180808*T*0353*Z*	1.00–1.80	0.60
$g^{(2)}(r)$	20180808*T*2011*Z*	20180809*T*0350*Z*	1.00–1.81	0.74
$g^{(2)}(r)$	20180809*T*2311*Z*	20180810*T*0332*Z*	1.01–1.71	n.a.
$g^{(2)}(r)$	20180810*T*1940*Z*	20180811*T*0327*Z*	1.00–1.70	1.19

a single telescope, as in Guerin et al. (2017), which serves as the zero-baseline visibility calibration. We do both in the following.

3.1 H α spectrum of P Cyg and expected temporal correlation

Thanks to its strong H α emission line, P Cyg is a classical target for amateur spectroscopy, which enabled us to obtain a spectrum recorded only a few days after our observations in the ARAS spectral data base (ARAS 2018). This spectrum (resolution : 9000, 4053 Å $< \lambda <$ 7763 Å) was recorded by J. Guarro i Fló on 2018 August 14.

We show in Fig. 2(a) the measured spectrum centred on the H α line, as well as the transmission spectrum of the 1 nm filter set in the CA, as provided by the manufacturer. Multiplying the two spectra, we obtain the spectrum of the detected light (Fig. 2b). Note that at this scale, the variation with the wavelength of the other elements (reflectivity of mirrors, transmission of the atmosphere and of the dichroic plate, quantum efficiency of the detectors) is negligible.

From the filtered spectrum, one can numerically compute the $g^{(2)}(\tau)$ function by using equations (2) and (3). This theoretical $g^{(2)}(\tau)$ function has a 100 per cent contrast and a width on the order of the picosecond (Fig. 2c). Experimentally we measure this function convolved by the response of the instrument, dominated by the jitter of the SPADs. The resulting expected $g^{(2)}(\tau)$ function is depicted in Fig. 2(d). Note the change of scales compared to Fig. 2(c). The expected contrast is now $C_0 = 3.8 \times 10^{-3}$.

3.2 Measured temporal correlation

We present in this section the measurement of $g^{(2)}(\tau)$ with a single telescope observing P Cyg. In this configuration the flux collected by the telescope is separated into two SPADs in order to overcome the dead time of the detectors (Guerin et al. 2017). This leads to some spurious correlations due to optical and electronic cross-talk between the detectors. These spurious correlations have to be characterized with a white source, for which the expected $g^{(2)}(\tau)$ function is flat, and then removed from the signal (Guerin et al. 2017). The 'white' signal has been measured in the lab after the observing run with a similar count rate.

The count rate was in average 3.8×10^5 counts per second (hereafter cps) per detector. The total observation time on P Cyg was 14 h over four nights (Table 1). The obtained $g^{(2)}(\tau)$ functions are shown in Fig. 3, with the direct measurements (P Cyg and

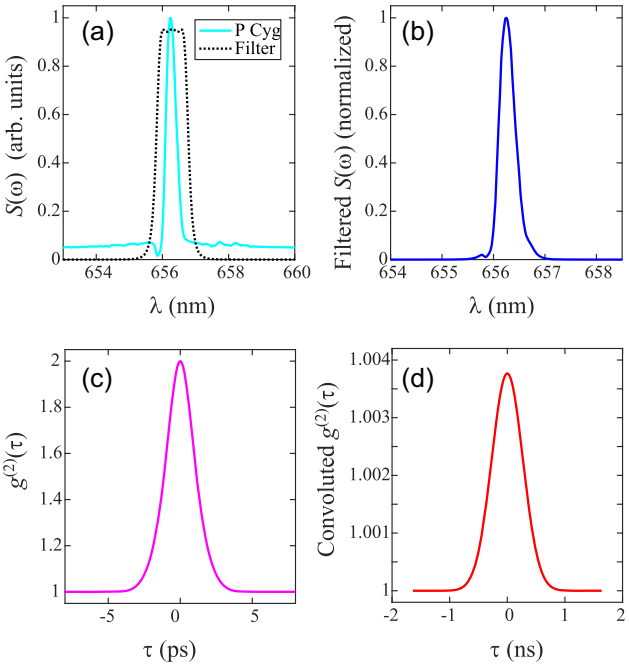

Figure 2. Spectrum and $g^{(2)}(\tau)$ function. (a) Spectrum of P Cyg zoomed-in on the H α emission line and transmission spectrum T of the filter (simulations provided by the manufacturer). (b) Filtered spectrum computed by multiplying the spectra of the star and of the filter. (c) Computed $g^{(2)}(\tau)$ from the filtered spectrum using equations (2) and (3) and supposing maximum visibility. (d) Convoluted $g^{(2)}(\tau)$ with the timing resolution of our acquisition chain. We have taken a Gaussian jitter of 450 ps (FWHM) per detector.

'white') in panel (a), and the corrected correlation function (after division by the 'white' signal to remove the spurious correlations) in panel (b).

The height of the bunching peak, defined as the maximum of the peak, is $C = (4.8 \pm 0.9) \times 10^{-3}$, in fair agreement with the expectation (Fig. 2d) given the uncertainty, estimated from the *rms* noise in the flat areas of the $g^{(2)}(\tau)$ function. Note that a small systematic effect may also be present due to an imperfect removing of spurious correlations and explain a slightly higher value than

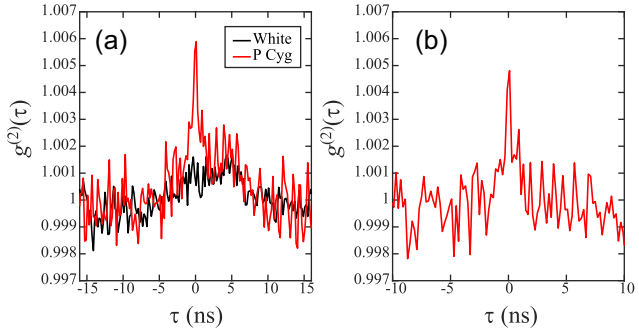

Figure 3. Measured temporal intensity correlation function. (a) Signal on the star and 'white' acquired in the lab. (b) $g^{(2)}(\tau)$ after removing the spurious correlations. The binning is 200 ps.

expected ($C_0 = 3.8 \times 10^{-3}$). For this reason, in Section 5.3.2, we will use the computed C_0 value to normalize the visibility data.

Besides providing a zero-baseline calibration for the spatial correlation measurement detailed in the next section, another important aspect of this temporal correlation experiment on an emission line is that the resulting $g^{(2)}(\tau)$ function provides information on the emission line itself via the contrast $C \sim \tau_c/\tau_{el}$. Knowing the response function of the instrument (and thus τ_{el}) and with some assumption on the shape of the line, we can deduce the width $\Delta\lambda$ of the emission line via $\tau_c = \lambda_0^2/c\Delta\lambda$. Here, approximating the line shape by a Gaussian, the temporal correlation measurement corresponds to a line width of FWHM $\Delta\lambda \simeq 0.3$ nm, in agreement with the actual spectrum. Note also that the contrast of the $g^{(2)}(\tau)$ function measured here is significantly higher than what it would be if it were determined by the 1-nm filter (the contrast would be $\sim 1.4 \times 10^{-3}$), which would be the case in the continuum (Guerin et al. 2017). This 'intensity-correlation spectroscopy' technique (Goldberger, Lewis & Watson 1966; Phillips, Kleinman & Davis 1967; Tan & Kurtsiefer 2017) would be relevant for exotic, very narrow lines, that would be hard to characterize with standard spectroscopic techniques. With intensity correlation, the narrower the line, the higher the contrast.

4 SPATIAL INTENSITY CORRELATION

We now turn to the spatial correlation experiment, performed with two nearly identical telescopes separated by 15 m on an East–West basis (Guerin et al. 2018). The flux collected at each telescope is filtered and coupled to the MMF with an identical CA and detected by a SPAD. The count rate per detector was in average 8.8×10^5 cps with a total acquisition time of 27 h over five nights (Table 1).

The cross-correlation between the arrival time of photons at the two detectors is computed in real time by the TDC using exposure times of 10 s. After the acquisition, the $g^{(2)}(\tau)$ functions are averaged together after being time shifted from the computed sidereal optical delay between the telescopes (Guerin et al. 2018).

Since the projected baseline also changes due to the Earth's rotation, several partial averaging of the data as a function of the computed baseline allow us to obtain several $g^{(2)}(\tau)$ functions for different projected baselines. Here, the limited signal-to-noise ratio of the data allows us to obtain only two significant curves, for projected baseline $9.5 < r < 12$ m and $12 < r < 15$ corresponding, respectively, to averaged baselines of 10.7 and 13.9 m. These measurements are reported in Fig. 4(b,c), along with the single-telescope correlation function (Figs 3b and 4a) for comparison.

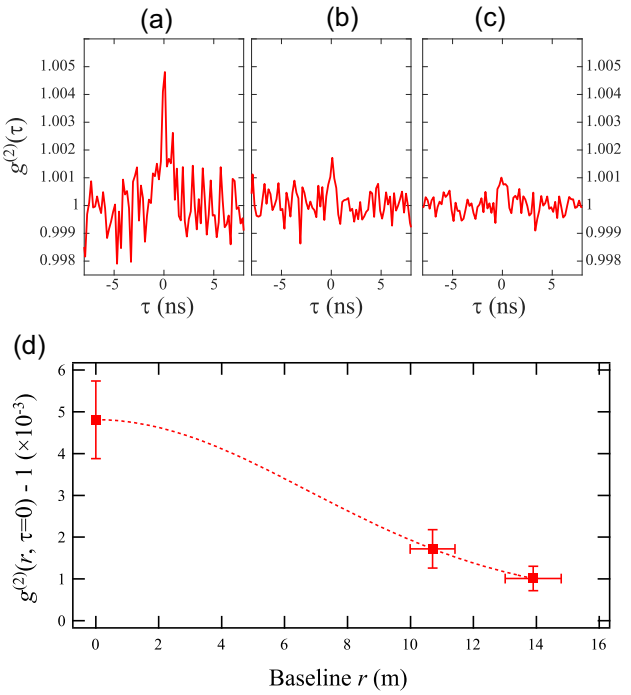

Figure 4. Top row, experimental curves $g^{(2)}(\tau)$ for different baselines: (a) single telescope experiment; (b) two-telescope data for all baselines $r < 12$ m, the average baseline is $r = 10.7$ m; (c) the same for $r > 12$ m, average baseline $r = 13.9$ m. (d) Contrast of the $g^{(2)}(\tau)$ function as a function of the baseline. The vertical error bars indicate the rms noise and the horizontal error bars the rms width of the distribution of projected baselines during the integration time, neglecting the aperture of the telescopes. The line is only a guide to the eye.

The effect of the partial resolution of P Cyg's emitting envelope is well visible via the contrast of the $g^{(2)}(\tau)$ function, which is much smaller. This contrast, plotted as a function of the baseline, gives the spatial intensity correlation function $g^{(2)}(r, \tau = 0)$, plotted in Fig. 4(d). This contrast gives the squared visibility $|V(r)|^2$ (equation 2) after proper normalization, such that $|V(0)|^2 = 1$ at zero baseline. We can use two normalization methods. The most direct method is to divide the contrast measured at $r \neq 0$ by the contrast measured with a single telescope ($r \approx 0$). However, the statistical noise as well as any systematic noise due to residual spurious correlations affect the results. The other method is to make use of the measured spectrum and, knowing the temporal resolution of the detection chain, compute the expected zero-baseline contrast, see Fig. 2(d). This method introduces much less noise but relies on the good characterization of the instrumental setup (filter and temporal resolution), which can be done in the lab. We show the results of the two methods in Table 2 and use the spectrum-based method in Fig. 7 at the end of the next section.

5 MODEL OF P CYG AND COMPARISON WITH THE EXPERIMENT

5.1 Atmosphere models: code CMFGEN

In order to analyse the visibility curve of P Cyg, we used state-of-the-art atmosphere models computed with the non-LTE (local thermodynamic equilibrium) radiative transfer code CMFGEN (Hillier & Miller 1998). It solves the coupled problem of the radiative transfer, statistical, and radiative equilibrium equations

Table 2. Summary of the observation results. r is the average projected baseline (its uncertainty is the rms width of the baseline distribution), T is the total integration time, F is the detected count rate per detector averaged over the total integration time. It is roughly twice lower in the single-telescope experiment because the flux has to be divided into two detectors. The contrast $C = g^{(2)}(0) - 1$ is the value of the correlation at zero delay given by the amplitude of the bunching peak, its uncertainty is the rms noise on the data. The two last columns correspond to the two possible normalization methods ($C_0 = 3.8 \times 10^{-3}$ is the zero-baseline contrast expected from the measured spectrum).

r (m)	T (h)	F ($\times 10^3$ cps)	$C(r)$ ($\times 10^{-3}$)	$C(r)/C(0)$	$C(r)/C_0$
0	14.5	380	4.80 ± 0.93	1	1.26 ± 0.24
10.7 ± 0.7	8	826	1.72 ± 0.46	0.36 ± 0.12	0.45 ± 0.12
13.9 ± 0.9	19	905	1.01 ± 0.29	0.21 ± 0.07	0.27 ± 0.08

in a spherically symmetric outflow. CMFGEN has been widely used in the literature to analyse central stars of planetary nebula (Marcolino et al. 2007), OB-type (Bouret et al. 2012), LBV (Groh et al. 2012), Wolf–Rayet stars (Tramper et al. 2013), and also core-collapse supernovae (Dessart et al. 2016). It includes, for example, effects of line-blanketing, wind clumping, and Auger ionization by X-rays, thus providing realistic spectra for hot stars from the ultraviolet (UV) to the mid-IR.

The code requires an initial estimate of the hydrostatic structure. For this purpose, we used the BSTAR2006 (Lanz & Hubeny 2007) grid of non-LTE plane-parallel models calculated with the code TLUSTY (Hubeny & Lanz 1995). This grid provides pure-photospheric models with effective temperature $15\,000\ \mathrm{K} \leq T_{\mathrm{eff}} \leq 30\,000\ \mathrm{K}$ and surface gravity $1.75 \leq \log(g) \leq 3.00$. Up to date, CMFGEN does not allow to calculate hydrodynamically self-consistent models, thus the wind velocity needs to be parametrized. For the wind, we employed a standard β velocity law

$$v(r) = v_\infty \left(1 - \frac{R_\star}{r}\right)^\beta, \tag{4}$$

where $R_\star$ is the stellar radius and v_∞ is the wind terminal velocity. The wind velocity structure is smoothly connected to the hydrostatic structure just above the sonic point.

Clumping was included by default in the models. In CMFGEN, a volume filling factor is used to parametrize the effect of clumping (microclumping approximation) in the wind density structure as follows,

$$f(r) = f_\infty + (1 - f_\infty)\mathrm{e}^{-\frac{v(r)}{v_{\mathrm{initial}}}}, \tag{5}$$

where v_{initial} is the onset velocity of clumping, corresponding to the distance in the wind where inhomogeneity starts to be relevant, and f_∞ is the filling factor value at $r \to \infty$. Thus, the density structure is parametrized, including the factor $f(r)$, as follows ($\dot{M}$ is the mass-loss rate):

$$\rho(r) = \frac{\dot{M}}{4\pi r^2 v(r) f(r)}. \tag{6}$$

We did not include Auger ionization by X-rays in the models since P Cyg is known to present a very low X-ray luminosity. The X-ray survey on Galactic LBVs of Nazé, Rauw & Hutsemékers (2012) could just provide an upper limit of $\log(L_{\mathrm{X}}/L_{\mathrm{BOL}}) < -9.4$ for P Cyg, including this star in their sub-sample for non-detection of X-ray emission. For comparison, O-type stars typically present $\log(L_{\mathrm{X}}/L_{\mathrm{BOL}}) \sim -7.0$ (Rauw et al. 2015).

Table 3. Number of levels, super-levels, and bound–bound transitions for each atomic species included in our CMFGEN reference model.

Ion	Full-levels	Super-levels	b–b transitions
H I	30	30	435
He I	69	69	905
He II	30	30	435
C II	100	44	1064
C III	99	99	5528
C IV	64	64	1446
N I	104	44	855
N II	144	62	1401
N III	287	57	6223
O I	90	35	615
O II	123	54	1375
O III	104	36	761
Mg II	44	36	348
Al II	44	26	171
Al III	65	21	1452
Si II	62	34	365
Si III	50	50	232
Si IV	66	66	1090
S II	88	27	796
S III	41	21	177
S IV	92	37	708
Ca II	19	12	65
Fe II	510	111	7357
Fe III	607	65	5482
Fe IV	1000	100	25 241
Fe V	1000	139	25 173

5.2 Stellar and wind parameters

CMFGEN is well suited for analysing P Cyg since previous spectroscopic and interferometric studies showed that its wind is almost spherical (see Section 1). Following the approach of Richardson et al. (2013), we analysed CMFGEN models based on the stellar and wind parameters derived by Najarro (2001). Also using CMFGEN, Najarro (2001) performed a detailed multiwavelength spectroscopic analysis of P Cyg from the UV up to the mid-IR region.

In Table 3, we show the atomic species included in the models together with the number of energy levels[1] and bound–bound transitions. These model atoms are similar to those used by Najarro (2001), providing a rather robust model to reproduce the spectrum of

[1] Super-level approach (grouping of energy levels) is introduced in CMFGEN for a faster computational treatment. See Hillier & Miller (1998) for further details.

Table 4. Summary of the main stellar and wind parameters of our CMFGEN reference model.

$L_\star$ ($L_\odot$)	610 000
$T_{\rm eff}$ (K)	18 700
$\log g$	2.25
$R_\star$ ($R_\odot$)	75
$M_\star$ ($M_\odot$)	37
$\dot{M}$ ($M_\odot\,{\rm yr}^{-1}$)	4.0×10^{-5}
f_∞	0.5
v_∞ ($km\,s^{-1}$)	185
β	2.3

P Cyg in the UV, visible, and IR regions. We also assumed the same chemical abundances as Najarro (2001). Since P Cyg has ended the hydrogen core-burning phase (Langer et al. 1994), the assumption of solar chemical abundances ($Z_\odot$) must overestimate the intensity in the Hα line (considering a fixed set of physical parameters in the model). Most important for the comparison with the observed visible spectrum, the abundances of H, He, C, N, and O were set to 0.66, 1.86, 0.31, 6.5, and 0.18 $Z_\odot$, respectively.

In Table 4, we present the physical stellar and wind parameters of our CMFGEN reference model. These are the main parameters to define the atmosphere model: stellar luminosity ($L_\star$), effective temperature ($T_{\rm eff}$), gravity surface acceleration ($\log g$), radius ($R_\star$), mass ($M_\star$), mass-loss rate ($\dot{M}$), wind clumping factor (f_∞), terminal velocity (v_∞), and the wind velocity law exponent (β). Except for the surface gravity $\log g$, all the other parameters are equal or close to the ones derived by Najarro (2001). We set $\beta = 2.3$ in our reference model due to numerical issues with $\beta = 2.5$ (Najarro 2001). As will be discussed in Section 5.3.1, we set $\dot{M} = 4.0 \times 10^{-5}\,M_\odot\,{\rm yr}^{-1}$ instead of $\dot{M} = 2.4 \times 10^{-5}\,M_\odot\,{\rm yr}^{-1}$ (Najarro 2001). Instead of $\log g = 1.20$, as in Najarro (2001), we assumed $\log g = 2.25$ since this is the lower value of $\log g$ in the TLUSTY models, according to the used effective temperature ($T_{\rm eff} = 18\,700$ K). Nevertheless, as pointed out by de Jager (2001), the determination of this parameter for P Cyg is quite uncertain, with a discrepancy up to a factor of 10 from different works in the literature. For example, Pauldrach & Puls (1990) derived 2.04 for the surface gravity of P Cyg.

5.3 Results of the simulations

5.3.1 Comparison to spectroscopic data

Before analysing our interferometric data, we compare, in Fig. 5, the synthetic spectrum calculated from our CMFGEN reference model (Tables 3 and 4) to the observed spectrum of P Cyg in the visible region, obtained from the ARAS Spectral Data Base. This comparison allows a physical validation, in terms of the spectroscopic appearance, of our adopted atmosphere model. Due to the effect of radial velocity, the observed spectrum was shifted in wavelength in order to match the synthetic spectrum.

Fig. 5 shows that our reference model is able to reproduce well the observed visible spectrum of P Cyg, showing intense P Cygni profiles in the Balmer and helium lines. Overall, the weak spectral features due to metals, such as C II λλ6580 and 6585 (close to Hα), are also fairly reproduced. Initially, we assumed the same value for the mass-loss rate as Najarro (2001), i.e. $\dot{M} = 2.4 \times 10^{-5}\,M_\odot\,{\rm yr}^{-1}$ with $f_\infty = 0.5$. Since the emission component of Hα is highly sensitive to the variation of the mass-loss rate, we followed the simplest approach of only varying this fundamental parameter of the wind. The Balmer lines, in particular Hα, seems to be better

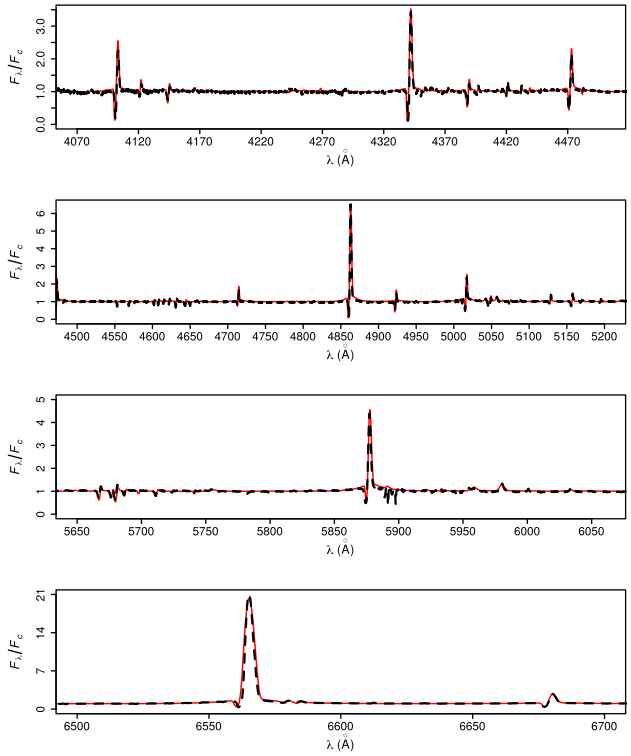

Figure 5. Comparison between the observed spectrum of P Cyg (black dashes) and the spectrum of the CMFGEN reference model (red line) used to analyse the interferometric data. The mass-loss rate of our reference model ($\dot{M} = 4.0 \times 10^{-5}\,M_\odot\,{\rm yr}^{-1}$) is close to the one derived by Najarro (2001) of $\dot{M} = 2.4 \times 10^{-5}\,M_\odot\,{\rm yr}^{-1}$. This model provides a fairly reasonable overall match to the spectrum.

reproduced using a slightly higher value for the mass-loss rate ($\dot{M} = 4.0 \times 10^{-5}\,M_\odot\,{\rm yr}^{-1}$ with $f_\infty = 0.5$). This difference is encompassed by the typical uncertainties on $\dot{M}$ found from spectroscopic analysis of massive stars in literature (see e.g. de Almeida et al. 2019). In addition, it is very unlikely to have a physical cause, as this difference is much larger than the mass-loss rate variability of P Cyg (Markova et al. 2001).

It is beyond the scope of this paper to derive the stellar and wind parameters of P Cyg, as performed by Najarro (2001). Nevertheless, the ability of our CMFGEN reference model to reproduce the visible spectroscopic appearance of P Cyg makes us confident to adopt this model in order to interpret our II observed visibilities.

5.3.2 Comparison to normalized II visibilities

To compare the reference CMFGEN model of P Cyg to the normalized II visibilities, we need to compute the effective radial intensity profile $I_{\rm eff}(\varpi)$ corresponding to the observed spectral region within the Hα filter,

$$I_{\rm eff}(\varpi) = \frac{\int I(\lambda, \varpi) T(\lambda)\,{\rm d}\lambda}{\int T(\lambda)\,{\rm d}\lambda}, \tag{7}$$

where $I(\lambda, \varpi)$ is the 1D monochromatic specific intensity, provided by CMFGEN, as a function of the radial coordinate ϖ (impact parameter). The effective wavelength $\lambda_{\rm eff}$ corresponding to $I_{\rm eff}$ for the reference CMFGEN model is given by

$$\lambda_{\rm eff} = \frac{\int \lambda F(\lambda) T(\lambda)\,{\rm d}\lambda}{\int F(\lambda) T(\lambda)\,{\rm d}\lambda} = 6562.9\,\text{Å}. \tag{8}$$

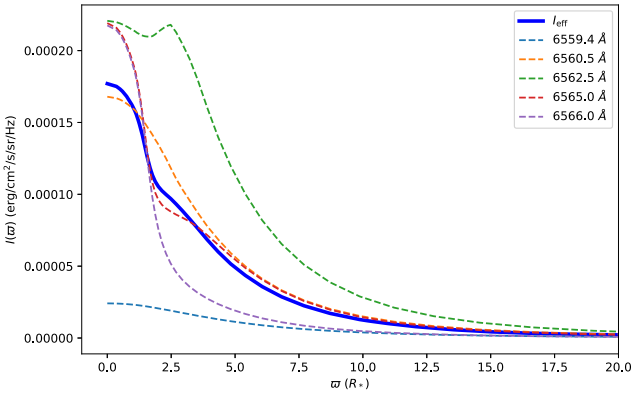

Figure 6. Effective H α radial profile $I_{\rm eff}(\varpi)$ (equation 7) of the reference CMFGEN model (thick solid blue) as a function of the radial coordinate ϖ given in units of the stellar photospheric radius (clipped at $20R_*$ for better visualization). For comparison, the dashed curves show the model specific intensity profiles $I(\lambda, \varpi)$ for selected wavelengths within the H α emission line and in the region where the filter transmission is high. In particular, we show the profile at $\lambda = 6562.5$ Å, nearly at the maximum of the model H α spectrum. We note that these selected profiles were not multiplied by the filter transmission.

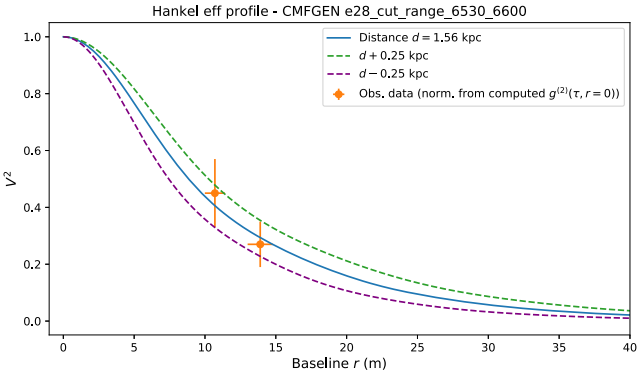

Figure 7. The data points are the measured squared visibility (Section 4) normalized by the contrast computed from the measured spectrum (Fig. 2d). They are fitted (solid blue line) using equation (9) with the distance d to P Cyg as the only free parameter (further details in the text). The curves correspond to the best-fitting d (solid) and associated $\pm 1\sigma$ uncertainties (dashed).

As before, $F(\lambda)$ and $T(\lambda)$ are the observed spectrum and the transmission filter, respectively (see Fig. 2). The effective H α radial profile $I_{\rm eff}(\varpi)$ of the reference CMFGEN model is shown in Fig. 6, together with radial profiles at some selected wavelengths for comparison.

The normalized squared visibility $|V|^2$ (or simply V^2) associated with the reference CMFGEN model is computed, thanks to the Hankel transform of $I_{\rm eff}(\varpi)$, normalized by the corresponding spectral flux, as

$$V^2 = \left| \frac{\int_0^\infty I_{\rm eff}(\rho) J_0(2\pi\rho q) 2\pi\rho \, {\rm d}\rho}{\int_0^\infty I_{\rm eff}(\rho) 2\pi\rho \, {\rm d}\rho} \right|^2, \quad (9)$$

where J_0 is the zeroth-order Bessel function of the first kind, $\rho = \varpi/d$ is the radial angular coordinate, with d being the distance to the target. The radial spatial frequency coordinate associated with ρ is $q = r/\lambda_{\rm eff}$, i.e. the II average projected baseline r divided by the effective wavelength of the observations $\lambda_{\rm eff}$. The Hankel transform is used here because of the circular symmetry of the model.

To interpret the II observations, we used the above equations to compute the V^2 corresponding to our reference CMFGEN model, which we assume to be a *bona fide* representation of P Cyg, since it well reproduces the observed visible spectrum, as shown in the previous subsection. Under this assumption, the only remaining free parameter is the distance d. We have thus used a PYTHON–SCIPY non-linear least-squares routine to fit the reference model V^2 to our II data, which allowed us to estimate the distance to P Cyg as $d = 1.56 \pm 0.25$ kpc. The fit has been performed on the visibility data normalized by the zero-baseline visibility computed from the measured spectrum (Fig. 2d and Table 2), as those data are less subjected to spurious correlations than the measured single-telescope correlation function. The latter has thus not been used. The observed and best-fitting model V^2 is shown in Fig. 7. These results and the interpretation of the measured d are discussed in the following section.

6 DISCUSSION AND CONCLUSION

P Cyg, together with η Car, are the brightest and most studied LBV stars for their spectrometric and photometric observational aspects, which have largely served to determine their physical properties (Najarro 2001). More recently, high angular resolution data, especially from long-baseline interferometry, have shed a new light on the fine spatial details of their mass-loss and geometries in general (Weigelt et al. 2007). As for P Cyg, GI2T, NPOI, and CHARA interferometers provided valuable estimates of the star parameters at the level of mas or a few mas angular resolutions. Although their results agree qualitatively, the numbers differ on the extent of the H α emitting envelope, for instance, which might be due to the variability of P Cyg on time-scales of a few months to year.

The method to determine the extent of P Cyg has often used analytical models such as uniform, limb-darkened discs or multiple Gaussians, whilst authors adopt distance values from different techniques, e.g. O–B association membership (Lamers, de Groot & Cassatella 1983; Turner et al. 2001), to interpret measured visibility points. The distance controversy for P Cyg is well known, with distances determined from ∼1.2 kpc up to 2.3 kpc (see e.g. table 1 of Turner et al. 2001). For instance, CHARA studies (Richardson et al. 2013) adopted a 1.7 kpc distance of P Cyg to match synthetic visibilities based on the CMFGEN stellar atmospheric model and basic parameters (Najarro 2001) to their observed visibilities. The more accurate distance for P Cyg, $d_{\rm G} = 1.36 \pm 0.24$ kpc, from the *Gaia* global astrometry mission and its second data release DR2 (Gaia Collaboration et al. 2018), could also be used. However, *Gaia* has been designed for sources fainter than 11th magnitude in the visible, where the parallax determination is limited by the photon noise. P Cyg has a visual magnitude of 4.5, which is too bright for the normal scanning operation at the focal detector of *Gaia* (Mignard, private communication). Therefore, the question of the exact parallax of P Cyg remains a real issue.

In this context, we have followed a different route by fixing the linear size of P Cyg in agreement with detailed multi wavelength spectroscopic studies in the literature (see Section 5). Our adopted model reproduces fairly well several lines of different atomic species, allowing us to adopt the linear radius of P Cyg photosphere as 75 $R_\odot$ and deliver synthesized visibilities and finally determine the distance of P Cyg as $d_{\rm II} = 1.56 \pm 0.25$ kpc. Note that for

such an approach to be effective, it would be useful to monitor interferometric measurements by simultaneous (and preferably *U*, *B*, *V*) photometry. For P Cyg, the variability can originate from effective temperature and radius changes of 10 per cent and 7 per cent, respectively, as concluded by Markova et al. (2001).

With this rather unusual interpretation of long baseline interferometry data, we propose a method to check and improve the so-called *wind momentum versus luminosity relation* (W-LR hereafter) introduced by Kudritzki, Lennon & Puls (1994), which relates the momentum flow of the wind from the star to its linear size times its luminosity,

$$\dot{M} v_\infty \propto R_\star^{-1/2} L_\star^{-1/\alpha_{\rm eff}}, \tag{10}$$

where $\alpha_{\rm eff}$ reflects all the spectral lines that drive the wind, with a typical value of 2/3, varying according to the spectral type (see e.g. table 2 of Kudritzki & Puls 2000).

The W-LR method consists in recording medium- or high-resolution spectra of the most luminous stars such as O, B, A supergiants, B[e] and LBV stars of the nearby galaxies, or the local Universe if possible, and determine their intrinsic luminosity from quantitative spectroscopy. Despite the good agreement between the theoretical and empirical (derived from spectroscopic analyses) W-LR for the most luminous massive stars (as the ones mentioned above), O-type dwarfs and giants with $\log L_\star/L_\odot \leq 5.2$ present much lower values of mass-loss rate, up to two orders of magnitude, than the theoretical values, affecting the WL-R (Martins et al. 2005; Marcolino et al. 2009; de Almeida et al. 2019). This shows the current need to check independently the WL-R.

To our knowledge, CMFGEN radiative transfer code represents a robust model to carry such a quantitative spectroscopy of the most luminous stars with their emission lines that often possess P Cyg profiles, i.e. a strong emission red wing and a blue absorption component corresponding to the projection of the wind components on the line of sight. The comparison of the apparent magnitude to the absolute luminosity would then estimate the distance of the luminous star to us even at Megaparsec levels.

As suggested by Vakili et al. (1998), such a method could be further improved by carrying the quantitative spectroscopy of a star observed by long-baseline interferometry and matching synthesized visibilities based on linear diameter of the star versus the measured visibility so as to determine the star's distance. This approach could be furthermore improved by observing luminous stars of Magellanic Clouds with different chemical abundances, i.e. Large Magellanic Cloud versus Short Magellanic Cloud. The brightest stellar members of Magellanic Clouds have apparent magnitudes in the range of 12–15 in the visible and their visibilities could be measured with future extremely long-baseline optical interferometers such as the intensity interferometric mode of the CTA array (Dravins 2016) or connecting large optical telescopes on existing observatories (Lai et al. 2018), such as Mauna Kea or Paranal, which will offer better than 10 μas angular resolution, compatible with the range of angular diameters of the brightest stars of the Magellanic Clouds. Therefore, this work constitutes the first successful step towards settling the quantitative spectroscopy of luminous stars and the W–LR relation, which may serve as an independent calibration technique of cosmological distances comparable to the Cepheid or post-AGB methods (Whitelock 2012).

ACKNOWLEDGEMENTS

We thank P. Weiss for participating in the observations, G. Labeyrie for fruitful discussions, and the MéO Team (Géoazur Laboratory) for their hospitality and help during the tentative session in 2018 November. We also thank F. Thévenin, P. Bério, and the Observatoire de la Côte d'Azur for financial support. We acknowledge the CATS team (Calern Atmospheric Turbulence Station, https://cats.oca.eu/) for providing turbulence real-time measurements and Swabian Instruments for very reactive technical support. We are also grateful to the ARAS data base community members, especially to J. Guarro i Flô, for their high quality spectra of P Cyg. This work is supported by the UCA-JEDI project ANR-15-IDEX-01, the Doeblin Federation, and the OPTIMAL platform. ESGdeA thanks OCA and the 'Ville de Nice' (Nice, France) for the financial support to this work through the 'Bourse Doctorale Olivier Chesneau' during the period of 2016–2019. In memorium of Paul Nuñez with whom all this adventure started in 2014.

REFERENCES

Acciari V. A. et al., 2020, MNRAS, 491, 1540
ARAS, 2018, ARAS Spectral Database. Public data available at: http://www.astrosurf.com/aras/.
Aristidi E., Fanteï-Caujolle Y., Ziad A., Dimur C., Chabé J., Roland B., 2014, in Stepp L. M., Gilmozzi R., Hall H. J., eds, Proc. SPIE Conf. Ser. Vol. 9145, Ground-based and Airborne Telescopes V. SPIE, Bellingham, p. 91453G
Balan A., Tycner C., Zavala R. T., Benson J. A., Hutter D. J., Templeton M., 2010, AJ, 139, 2269
Bouret J. C., Hillier D. J., Lanz T., Fullerton A. W., 2012, A&A, 544, A67
Chabé J., Ziad A., Fanteï-Caujolle Y., Aristidi E., Renaud C., Blary F., Marjani M., 2016, in Hall H. J., Gilmozzi R., Marshall H. K., eds, Proc. SPIE Conf. Ser. Vol. 9906, Ground-Based and Airborne Telescopes VI. SPIE, Bellingham, p. 99064Z
Chesneau O. et al., 2000, A&AS, 144, 523
de Almeida E. S. G., Marcolino W. L. F., Bouret J. C., Pereira C. B., 2019, A&A, 628, A36
de Jager C., 2001, in de Groot M., Sterken C., eds, ASP Conf. Ser. Vol. 233, P Cygni 2000: 400 Years of Progress. Astron. Soc. Pac., San Francisco, p. 215
Dessart L., Hillier D. J., Audit E., Livne E., Waldman R., 2016, MNRAS, 458, 2094
Dravins D., 2016, in Malbet F., Creech-Eakman M. J., Tuthill P. G., eds, Proc. SPIE Conf. Ser. Vol. 9907, Optical and Infrared Interferometry and Imaging V. SPIE, Bellingham, p. 99070M
Gaia Collaboration, 2018, A&A, 616, A1
Goldberger M. L., Lewis H. W., Watson K. M., 1966, Phys. Rev., 142, 25
Groh J. H., Hillier D. J., Madura T. I., Weigelt G., 2012, MNRAS, 423, 1623
Guerin W., Dussaux A., Fouché M., Labeyrie G., Rivet J.-P., Vernet D., Vakili F., Kaiser R., 2017, MNRAS, 472, 4126
Guerin W., Rivet J.-P., Fouché M., Labeyrie G., Vernet D., Vakili F., Kaiser R., 2018, MNRAS, 480, 245
Hanbury Brown R., 1974, The Intensity Interferometer: Its Application to Astronomy. Taylor & Francis, London
Hanbury Brown R., Twiss R. Q., 1956, Nature, 178, 1046
Hanbury Brown R., Davis J., Herbison-Evans D., Allen L. R., 1970, MNRAS, 148, 103
Hanbury Brown R., Davis J., Allen L. R., 1974, MNRAS, 167, 121
Herbison-Evans D., Hanbury Brown R., Davis J., Allen L. R., 1971, MNRAS, 151, 161
Hillier D. J., Miller D. L., 1998, ApJ, 496, 407
Hubeny I., Lanz T., 1995, ApJ, 439, 875
Kieda D. et al., 2019a, State of the Profession: Intensity Interferometry, Astro2020 Science White Paper, p. 227
Kieda D. et al., 2019b, Science Opportunities Enabled by the Era of Visible Band Stellar Imaging with Sub-100 μarc-sec Angular Resolution, Astro2020 Science White Paper, p. 275
Kudritzki R.-P., Puls J., 2000, ARA&A, 38, 613

Kudritzki R., Lennon D., Puls J., 1994, in Walsh J., Danziger I., eds, Proceedings of the ESO Workshop, Science with the VLT. Springer, Berlin, p. 246
Labeyrie A., Lipson S. G., Nisenson P., 2006, An Introduction to Optical Stellar Interferometry. Cambridge Univ. Press, Cambridge
Lai O. et al., 2018, in Creech-Eakman M. J., Tuthill P. G., Mérand A., eds, Proc. SPIE Conf. Ser. Vol. 1070, SPIE Astronomical Telescopes + Instrumentation. SPIE, Bellingham, p. 1070121
Lamers H., de Groot M., 1992, A&A, 535, A67
Lamers H. J. G. L. M., de Groot M., Cassatella A., 1983, A&A, 128, 299
Langer N., Hamann W. R., Lennon M., Najarro F., Pauldrach A. W. A., Puls J., 1994, A&A, 290, 819
Lanz T., Hubeny I., 2007, ApJS, 169, 83
Loudon R., 1973, The Quantum Theory of Light. Oxford Science Publications, Oxford
Marcolino W. L. F., Hillier D. J., de Araujo F. X., Pereira C. B., 2007, ApJ, 654, 1068
Marcolino W. L. F., Bouret J. C., Martins F., Hillier D. J., Lanz T., Escolano C., 2009, A&A, 498, 837
Markova N. et al., 2001, A&A, 376, 898
Martins F., Schaerer D., Hillier D. J., Meynadier F., Heydari-Malayeri M., Walborn N. R., 2005, A&A, 441, 735
Matthews N., LeBohec S., 2019, in PoS 358, 740, 36th International Cosmic Ray Conference, Sissa Medialab, Trieste, Italy
Najarro F., 2001, in de Groot M., Sterken C., eds, ASP Conf. Ser. Vol. 233, P Cygni 2000: 400 Years of Progress. Astron. Soc. Pac., San Francisco, p. 133
Najarro F., Hillier D. J., Stahl O., 1997, A&A, 326, 1117
Nazé Y., Rauw G., Hutsemékers D., 2012, A&A, 538, A47
Nota A., Livio M., Clampin M., Schulte-Ladbeck R., 1995, ApJ, 448, 788
Pauldrach A. W. A., Puls J., 1990, A&A, 237, 409
Phillips D. T., Kleinman H., Davis S. P., 1967, Phys. Rev., 153, 113
Pollmann E., Vollmann W., 2013, J. Am. Assoc. Var. Star Obs., 41, 24
Rauw G. et al., 2015, ApJS, 221, 1
Richardson N. D., Morrison N. D., Gies D. R., Markova N., Hesselbach E. N., Percy J. R., 2011, AJ, 141, 120
Richardson N. D. et al., 2013, ApJ, 769, 118
Rivet J.-P., Vakili F., Lai O., Vernet D., Fouché M., Guerin W., Labeyrie G., Kaiser R., 2018, Exp. Astron., 46, 531
Tan P. K., Kurtsiefer C., 2017, MNRAS, 469, 1617
Tramper F. et al., 2013, A&A, 559, A72
Turner D., Welch G., Graham M., Fairweather D., 2001, J. Am. Assoc. Var. Star Obs., 29, 73
Vakili F., Mourard D., Bonneau D., Morand F., Stee P., 1997, A&A, 323, 183
Vakili F., Mourard D., Stee P., Bonneau D., 1998, in Wolf B., Stahl O., Fullerton A., eds, Proc. IAU Colloquium No. 169, Variable and Non-spherical Stellar Winds in Luminous Hot Stars. Springer, Berlin, p. 87
Weigelt G. et al., 2007, A&A, 464, 87
Whitelock P. A., 2012, Astrophys. Space Sci., 341, 123
Ziad A., Borgnino J., Dali Ali W., Berdja A., Maire J., Martin F., 2012, J. Opt., 14, 045705

This paper has been typeset from a TEX/LATEX file prepared by the author.